

AN EXPLICIT SPECTRAL DECOMPOSITION OF THE ADRT

WEILIN LI*, KARL OTNESS†, KUI REN‡, AND DONSUB RIM§

Abstract. The approximate discrete Radon transform (ADRT) is a hierarchical multiscale approximation of the Radon transform. In this paper, we factor the ADRT into a product of linear transforms that resemble convolutions, and derive an explicit spectral decomposition of each factor. We further show that this implies—for data lying in the range of the ADRT—that the transform of an $N \times N$ image can be formally inverted with complexity $\mathcal{O}(N^2 \log^2 N)$. We numerically test the accuracy of the inverse on images of moderate sizes and find that it is competitive with existing iterative algorithms in this special regime.

Key words. approximate discrete Radon transform, fast algorithm, Radon transform, spectral decomposition

AMS subject classifications. 44A12, 65R10, 92C55, 68U05, 15A04

1. Introduction. The continuous Radon transform takes a function defined over the Euclidean plane and produces a new function over the space of all straight lines, assigning per line the value of the corresponding line integral of the original function [10, 13]. The approximate discrete Radon transform (ADRT) [5, 8, 16] is a fast algorithm for computing a multiscale discretization of the continuous Radon transform. ADRT is applicable in various contexts, in computerized tomography and inverse problems [13, 6], solutions to partial differential equations [7, 18], and in sliced Wasserstein barycenters or interpolants [4, 20], to name a few.

Given an $N \times N$ image with $N = 2^n$ for some positive integer n , the ADRT R^n transforms that image in $\mathbb{R}^{N \times N}$ to one in $\mathbb{R}^{4 \times N \times (\frac{3}{2}N - \frac{1}{2})}$ using $\mathcal{O}(N^2 \log N)$ floating point operations, and this transformed data is an approximation of the continuous Radon transform of that image. In this work, we derive a new spectral decomposition of ADRT, and demonstrate that the decomposition leads to a fast and explicit computation of the inverse of ADRT in the setting where the data lies in its range.

As we will illustrate below, the ADRT can be factored as

$$(1.1) \quad R^n = S_{(n)}^n S_{(n-1)}^n \cdots S_{(1)}^n$$

where $S_{(m)}^n$ for $m = 1, \dots, n$, represent summation operations at each multiscale level of ADRT corresponding to the length scale $\sim 2^{m-n}$. The main contribution of this work is the derivation of an explicit spectral decomposition of each of the factors,

$$(1.2) \quad S_{(m)}^n = U_{(m)}^n \Sigma_{(m)}^n V_{(m)}^{n\top}, \quad m = 1, 2, \dots, n,$$

which possesses certain desirable properties: (1) The matrices $U_{(m)}^n$ and $V_{(m)}^n$ are either orthogonal or contain orthogonal square subblocks of maximal size; (2) $\Sigma_{(m)}^n$ is

*Department of Mathematics, City College of New York, New York, NY 10031, USA (wli6@ccny.cuny.edu)

†Courant Institute of Mathematical Sciences, New York University, New York, NY 10012, USA (karl.otness@nyu.edu)

‡Department of Applied Physics and Applied Mathematics, Columbia University, New York, NY 10027, USA (kr2002@columbia.edu)

§Department of Mathematics, Washington University in St. Louis, St. Louis, MO 63130, USA (rim@wustl.edu)

diagonal with positive entries; and (3) the columns of $U_{(m)}^n$ and $V_{(m)}^n$ are each made up of columns of discrete sine transforms (DSTs) or discrete cosine transforms (DCTs), and the multiplication by these matrices or their transposes can be performed in $\mathcal{O}(N^2 \log N)$ operations.

We use a notation that resembles that for the singular value decomposition (SVD) for this decomposition since it is indeed the SVD of S_m^n for the levels $m > 1$, and it is a spectral decomposition with an SVD-like structure for the level $m = 1$. We will remind the reader of this distinction throughout.

The fact that discrete sine and cosine transforms make up these columns is not a complete surprise, considering how the Fourier slice theorem [13] relates the continuous Radon transform to the Fourier transform in a straightforward manner. However, in the discretized setting the image and the transformed data are represented as pixelated images on Cartesian grids, and as a result the precise relation between a discretized Radon transform and the discretized Fourier transform is not straightforward to pin down. The relation depends delicately on the choice of discretization; for example, the preservation of such a relation is an important consideration in the derivation of the digital Radon transform via pseudo-polar Fourier transforms [1, 2, 3]. The explicit decomposition we present here (1.2) establishes a precise discrete relation for the ADRT: since the columns are made up of DSTs or DCTs, one can equate the discrete transforms on the ADRT data to a variant of the discrete Fourier transform in the image domain. That is, our spectral decomposition implies a fully discrete version of the Fourier slice theorem that is specific to the ADRT.

The spectral decomposition is useful for inverting the ADRT. Given some ADRT data $b \in \mathbb{R}^{4 \times N \times (\frac{3}{2}N - \frac{1}{2})}$ lying in the range $b \in \text{range}(R^n)$, we consider the problem of finding $x \in \mathbb{R}^{N \times N}$ satisfying

$$(1.3) \quad R^n[x] = b.$$

Broadly speaking, most readers will be more interested in the general inverse problem $\min_x \|R^n[x] - b\|$ for some norm $\|\cdot\|$, without the assumption that $b \in \text{range}(R^n)$. While that general problem is outside the scope of this paper, it is important to note that the range characterization result [11] showed $\text{range}(R^n)$ to be highly structured. Exploiting this structure, it is potentially possible to numerically project the data b directly to $\text{range}(R^n)$, and the projection will reduce the general problem to our setting. Hence, we believe the results in this paper will be relevant to the general problem as well.

The decomposition (1.2) yields an explicit expression for the pseudo-inverse for each $S_{(m)}^n$. With the pseudo-inverses $S_{(m)}^{n\dagger}$ of individual levels $m = 1, \dots, n$ at hand, the inverse x satisfying (1.3) is given by

$$(1.4) \quad x = S_{(1)}^{n\dagger} \dots S_{(n-1)}^{n\dagger} S_{(n)}^{n\dagger} b.$$

Due to the block structures of $U_{(m)}^n$ and $V_{(m)}^n$ and due to their columns being expressed in terms of DSTs and DCTs, this pseudo-inverse can be computed in $\mathcal{O}(N^2 \log N)$ serial operations, or in $\mathcal{O}(N \lceil \frac{N}{P} \rceil \log N)$ operations with $P < N$ parallel processors. We will call this fast and explicit computation of the inverse, the *Spectral Pseudo-Inverse, Fast and Explicit*, (SPIFE) of ADRT.

SPIFE is exact if $b \in \text{range}(R^n)$ and if there were no errors in the floating point arithmetic. With finite-precision floating point arithmetic, the accuracy of SPIFE

depends on the precision and the size of the image. For double-precision and image sizes that are moderately small $N \leq 2^8$, this explicit inverse outperforms existing iterative inverses, the generic conjugate gradient (CG) algorithm [9] and the full multi-grid (FMG) inverse devised for the ADRT [16], in terms of accuracy per workload for the case. We will present numerical experiments demonstrating this performance.

We perform additional numerical experiments and explain why finite-precision SPIFE loses accuracy. As the pseudo-inverses are applied from right to left in (1.4), the floating point calculation errors accumulate in the levels $m > 1$ due to the large values in $(\Sigma_m^n)^{-1}$ appearing inside the pseudo-inverse $S_{(m)}^{n\dagger}$ and significant digits are progressively lost. An accurate image is recovered only if sufficient digits are retained before reaching level $m = 1$, at which point $S_{(1)}^{n\dagger}$ stabilizes the inverse by removing some of the unstable components. For a given precision level, this means the images sizes must not be too large.

A closely related fact is that the explicit inverse of cost $\mathcal{O}(N^2 \log N)$ for the single-quadrant ADRT is highly unstable [19, 16, 14]. This explicit single-quadrant inverse is—asymptotically as the resolution N increases—related to the limited-angle problem [12][13, Section VI.2] for the continuous Radon transform: that is, for a sequence of images $x_k \in \mathbb{R}^{N_k \times N_k}$ and data $b_k \in \mathbb{R}^{4 \times N_k \times (\frac{3}{2}N_k - \frac{1}{2})}$ that approaches a function and its Radon transform as $k \rightarrow \infty$, respectively, the inversion of the single-quadrant ADRT approaches a limited-angle problem. Due to this connection, the instability is inherent, and one does not generally expect to find numerical techniques for controlling it. In contrast, SPIFE is not inherently unstable, as it utilizes ADRT data from all four quadrants, and so asymptotically its stability should match that of the (full-angle) inversion of the continuous Radon transform; this inversion is only mildly ill-conditioned [13]. In this sense, one may view SPIFE as a stable extension of the naïve explicit single-quadrant inverse to the full “all-quadrants” ADRT. We provide a comparison in our experiments.

Previously, Press observed in his experimentation with the FMG inverse a certain scaling between the number of iterations and error reduction, and claimed that his FMG inverse would achieve a desired error threshold with $\mathcal{O}(N^2 \log^3 N)$ work [16]. Based on this observed scaling, he further conjectured that an iterative algorithm of $\mathcal{O}(N^2 \log^q N)$ with $2 \leq q \leq 3$ could exist and that $q = 2$ would be optimal. These complexity bounds were never rigorously proved, however. As for SPIFE, it has precisely the best conjectured complexity $\mathcal{O}(N^2 \log^2 N)$, and if (1) the provided data b lies in the range up to double precision, and (2) the image size is not large ($N \leq 2^8$), then the explicit pseudo-inverse computed with competitive accuracy. Hence, our result marks partial progress towards the conjecture of Press.

However, as mentioned above, the key practical motivation for studying the ADRT lies in the search of a faster inverse postulated in the unrestricted conjecture: an optimally fast Moore-Penrose inverse that is accurate up to the inherent conditioning of R^n regardless of the image size or whether the data lies in the range. The results here offer promise towards that goal. To achieve it, SPIFE must be aided by two further developments: (1) a fast projection algorithm that is able to orthogonally project the data to the range of the ADRT [11] to numerical precision, and (2) a stabilization technique that prevents numerical errors from accumulating when applying the pseudo-inverse. These topics will be pursued in future works.

2. Notations, preliminaries, and outline. We recall a few definitions and notations from [19, 11] then outline the key results of the paper.

2.1. Notation and preliminaries. Let \mathbb{Z} denote the integers, \mathbb{N}_0 the non-negative integers, and \mathbb{N} the natural numbers. Define a set of indices $[m] := \{i \in \mathbb{N}_0 \mid i < m\}$ for $m \in \mathbb{N}_0$, and $[m]_1 := \{i + 1 \mid i \in [m]\}$. For simplicity of notation, we will use members of $[m] \times [n]$ for row and column indexing of a matrix in $\mathbb{R}^{m \times n}$ in lieu of $[m]_1 \times [n]_1$ so that the indexing will start from 0 rather than 1. Id^n will denote the identity in $\mathbb{R}^{2^n \times 2^n}$ whereas Id_m the identity in $\mathbb{R}^{m \times m}$. Let us define the remainder $\% : \mathbb{N}_0 \times \mathbb{N}_0 \rightarrow \mathbb{N}_0$ given by $a \% b := a - \lfloor a/b \rfloor \cdot b$ if $b \neq 0$ and by $a \% b := a$ if $b = 0$.

To describe ADRT data, it is convenient to allow tuples of indices with negative values for each index, and to allow variable bounds for the index range.

We define the index set E_m^n as

$$(2.1) \quad E_m^n = \{(h, s) \in \mathbb{Z} \times [2^n] \mid -(s \% 2^m) \leq h < 2^n\}.$$

We partition E_m^n into subsets $E_{m,\ell}^n$,

$$(2.2) \quad E_m^n = \bigcup_{\ell \in [2^{n-m}]} E_{m,\ell}^n,$$

where $E_{m,\ell}^n$ is the restriction of the second index to the range $\ell 2^m + [2^m]$,

$$(2.3) \quad E_{m,\ell}^n = \{(h, s) \in \mathbb{Z} \times [2^n] \mid -(s \% 2^m) \leq h < 2^n, s \in \ell 2^m + [2^m]\}.$$

We further partition $E_{m,\ell}^n$ into subsets $E_{m,\ell,t}^n$

$$(2.4) \quad E_{m,\ell}^n = \bigcup_{t \in [2^m]} E_{m,\ell,t}^n,$$

where $E_{m,\ell,t}^n$ is the restriction of the second index to a single value

$$(2.5) \quad E_{m,\ell,t}^n = \{(h, s) \in \mathbb{Z} \times [2^n] \mid -(t \% 2^m) \leq h < 2^n, s = \ell 2^m + t\}.$$

Next, we define functions defined on these index sets $f \in \mathbb{R}^{E_m^n}$. Such a function can also be viewed as a matrix with suitable zero paddings, or an array of dimension two with variable column sizes. Let us define the restriction $f_{m,\ell}^n \in \mathbb{R}^{E_{m,\ell}^n}$ of $f \in \mathbb{R}^{E_m^n}$ as

$$(2.6) \quad f_{m,\ell}^n(h, s) := f(h, s + \ell 2^m), \quad (h, s) \in \mathbb{R}^{E_{m,\ell}^n},$$

and similarly the restriction $f_{m,\ell,t}^n \in \mathbb{R}^{E_{m,\ell,t}^n}$ of $f_{m,\ell}^n \in \mathbb{R}^{E_{m,\ell}^n}$ as

$$(2.7) \quad f_{m,\ell,t}^n(h) := f_{m,\ell}^n(h, t) = f(h, t + \ell 2^m), \quad (h, t) \in \mathbb{R}^{E_{m,\ell,t}^n}.$$

See [Figure 2.1](#) for an illustrative example.

The single-quadrant ADRT at the individual level m is denoted by

$$(2.8) \quad S_m^n : \mathbb{R}^{E_{m-1}^n} \rightarrow \mathbb{R}^{E_m^n}, \quad S_m^n[f] = g,$$

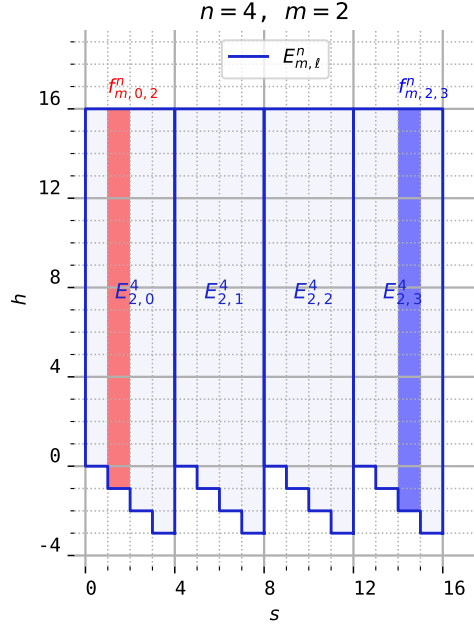


Fig. 2.1: An example of the vectors $f_{m,\ell,t}^n$, illustrating two different instances of these vectors and labeling the index sets for each of the four sections of the ADRT.

where for each $(h, s) \in E_{m-1,0}^n$ we let

$$(2.9) \quad \begin{aligned} g_{m,\ell}^n(h, 2s+1) &:= f_{m,2\ell}^n(h, s) + f_{m,2\ell+1}^n(h+s+1, s), \\ g_{m,\ell}^n(h, 2s) &:= f_{m,2\ell}^n(h, s) + f_{2\ell+1}^n(h+s, s). \end{aligned}$$

Now we set additional notations and definitions related to the full ADRT, as opposed to those related to the single-quadrant ADRT considered thus far. We distinguish the analogous mappings by putting a parenthesis around the level index m : For example, S_m^n denotes a single-quadrant ADRT level whereas $S_{(m)}^n$ denotes the full ADRT level.

DEFINITION 2.1. *The level m of the full ADRT for image $f \in \mathbb{R}^{2^n \times 2^n}$ is denoted by $S_{(m)}^n$ which we define separately for the case $m = 1$ and the case $m = 2, 3, \dots, n$.*

- For $m = 1$ we define $S_{(1)}^n : \mathbb{R}^{2^n \times 2^n} \rightarrow \mathbb{R}^{4 \times E_1^n}$ then let us define,

$$(2.10) \quad S_{(1)}^n := [S_1^n T_I^n, S_1^n T_{II}^n, S_1^n T_{III}^n, S_1^n T_{IV}^n]^\top,$$

where $T_I^n, \dots, T_{IV}^n : \mathbb{R}^{2^n \times 2^n} \rightarrow \mathbb{R}^{2^n \times 2^n}$ are permutations corresponding to the four quadrants I, ..., IV given by

$$(2.11) \quad \begin{cases} (T_I^n f)(i, j) = f(j, 2^n - 1 - i), \\ (T_{II}^n f)(i, j) = f(2^n - 1 - i, j), \\ (T_{III}^n f)(i, j) = f(i, j), \\ (T_{IV}^n f)(i, j) = f(2^n - 1 - j, 2^n - 1 - i), \end{cases} \quad i, j \in [2^n].$$

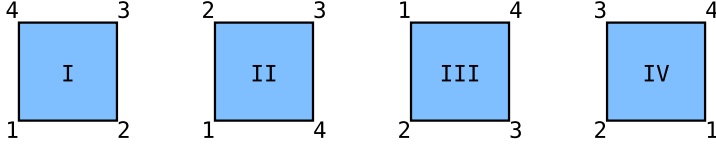


Fig. 2.2: The orientation of the four quadrants. The four corners are numbered to indicate the precise orientation, and the orientation of quadrant III matches that of the original image, that is, $T_{\text{III}}^n = \text{Id}^n$ (2.11).

We refer to the first level as the cross-quadrant level.

- For $m = 2, \dots, n$ let $S_{(m)}^n : \mathbb{R}^{4 \times E_{m-1}^n} \rightarrow \mathbb{R}^{4 \times E_m^n}$ with

$$(2.12) \quad S_{(m)}^n := \text{Id}_4 \otimes S_m^n,$$

that is, the block diagonal matrix,

$$(2.13) \quad S_{(m)}^n = \text{diag}[S_m^n, S_m^n, S_m^n, S_m^n].$$

We refer to these later levels single-quadrant levels.

See Figure 2.2 for a depiction of the orientation of the four quadrants.

Finally, $R_{(n)}^n$ will denote the full ADRT, as given by $R_{(n)}^n = S_{(n)}^n S_{(n-1)}^n \dots S_{(1)}^n$ (1.1). We sometimes often omit the subscript of $R_{(n)}^n$ and write R^n instead.

2.2. Outline. We provide an outline of this paper. As discussed in the introduction (Section 1), the main goal of this paper is to show that the individual level $S_{(m)}^n$ of the full ADRT (Definition 2.1) has a spectral decomposition in an explicit form (1.2). We first derive the decomposition of $S_{(m)}^n$ for levels $m > 1$ (2.12) in Section 3, which is given straightforwardly by the convolution theorem upon certain permutations. The decomposition of $S_{(m)}^n$ for level $m = 1$ (2.10) is more involved due to the presence of the rotations and reflections $T_{\text{I}}^n, \dots, T_{\text{IV}}^n$ in (2.11), but we show it is still possible to derive a spectral decomposition for this case in Section 4 by exploiting discrete directional patterns we devise.

An important consequence of this decomposition is that the inverse problem (1.3) can be solved efficiently using the pseudo-inverses of the $(S_{(m)}^n)_{m=1}^n$, assuming the supplied data b is in the range of R^n . We referred to this fast computational inverse as SPIFE in the Introduction, and it is defined in Section 5. Results from numerical experiments regarding SPIFE are reported in Section 6. Therein we provide comparisons with existing iterative inverse and detail numerical issues that arise when double precision floating point arithmetic is used in SPIFE.

3. SVD of single-quadrant levels ($m > 1$). In this section, we derive the explicit SVDs of each level of ADRT $S_{(m)}^n$ for levels $m > 1$. The result follows from the simple observation that, upon certain permutations, $S_{(m)}^n$ can be written as a block diagonal matrix, and the individual block is either a matrix representing a convolution or a transposed convolution. Then the SVD follows: For convolution and transposed

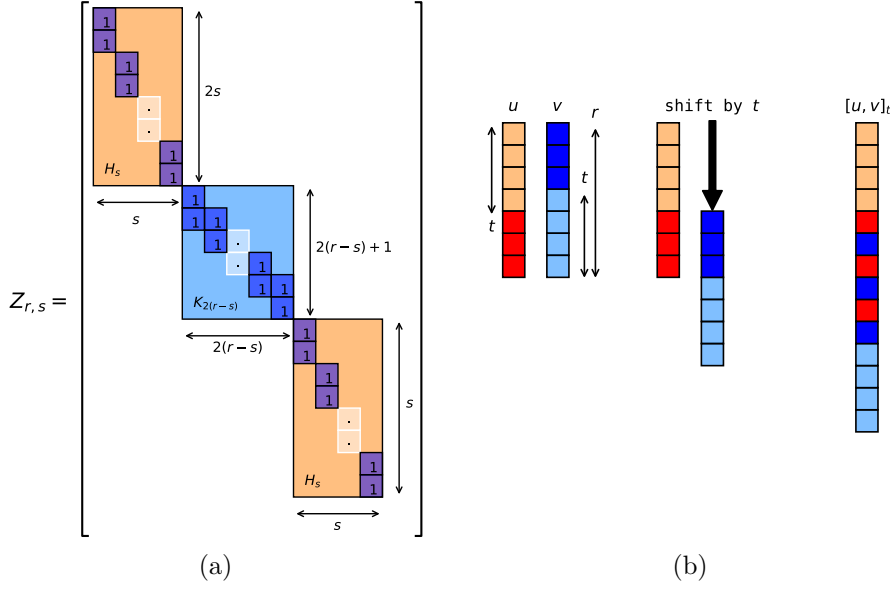


Fig. 3.1: (a) The blocks of matrix $Z_{r,s}$ (3.13), and (b) an illustration of $[u, v]_t$ for $u, v \in \mathbb{R}^r$ according to Definition 3.3.

Proof. Follows immediately due to Lemma 3.1 and the remarks above. \square

Let us define

$$(3.16) \quad Z_{m,0}^n := \text{diag} \left[\underbrace{Z_{N,0}, Z_{N,1}, \dots, Z_{N,2^{m-1}-1}}_{2^m \text{ blocks}} \right].$$

Then Lemma 3.1 implies,

$$\begin{aligned} Z_{m,0}^n &= \text{diag}[Z_{2^n,0}, Z_{2^n,1}, \dots, Z_{2^n,2^m-1}] \\ &= \text{diag}[U_{2^n,0} \Sigma_{2^n,0} V_{2^n,0}^\top, \dots, U_{2^n,2^m-1} \Sigma_{2^n,2^m-1} V_{2^n,2^m-1}^\top] \\ &= U_{m,0}^n \Sigma_{m,0}^n V_{m,0}^{n\top}, \end{aligned}$$

where

$$(3.17) \quad \begin{aligned} U_{m,0}^n &= \text{diag}[U_{2^n,0}, \dots, U_{2^n,2^m-1}], \\ \Sigma_{m,0}^n &= \text{diag}[\Sigma_{2^n,0}, \dots, \Sigma_{2^n,2^m-1}], \\ V_{m,0}^n &= \text{diag}[V_{2^n,0}, \dots, V_{2^n,2^m-1}]. \end{aligned}$$

As a result if we let,

$$(3.18) \quad Z_m^n := \text{Id}^{n-m-1} \otimes Z_{m,0}^n = \text{diag} \left[\underbrace{Z_{m,0}^n, Z_{m,0}^n, \dots, Z_{m,0}^n}_{2^{n-m-1} \text{ blocks}} \right],$$

and let

$$(3.19) \quad \begin{cases} U_m^n := \text{Id}^{n-m-1} \otimes U_{m,0}^n, \\ \Sigma_m^n := \text{Id}^{n-m-1} \otimes \Sigma_{m,0}^n, \\ V_m^n := \text{Id}^{n-m-1} \otimes V_{m,0}^n, \end{cases}$$

we obtain the SVD

$$(3.20) \quad Z_m^n = U_m^n \Sigma_m^n V_m^{n\top}.$$

Next, we will describe the permutations that will transform $S_{(m)}^n$ into convolutions. It will be handy to set a notation for a certain alternating concatenation of two vectors with shift.

DEFINITION 3.3 (Alternating concatenation with shift). *Given two vectors $u, v \in \mathbb{R}^r$ define a vector $[u \mid v]_t \in \mathbb{R}^{2r}$ with $t \in [r]$ be given by*

$$(3.21) \quad ([u \mid v]_t)_j := \begin{cases} u_j & \text{if } j \in [t], \\ u_{t+(j-t-1)/2} & \text{if } j-t \in [2r-t] \text{ and } j-t \text{ even}, \\ v_{\lfloor (j-t)/2 \rfloor} & \text{if } j-t \in [2r-t] \text{ and } j-t \text{ odd}, \\ v_{j-r} & \text{if } j-2r+t \in [t]. \end{cases}$$

The mapping $[\cdot \mid \cdot]_t : \mathbb{R}^r \times \mathbb{R}^r \rightarrow \mathbb{R}^{2r}$ is invertible, so we will denote the inverse operation $[\cdot]^{-1} : \mathbb{R}^{2r} \rightarrow \mathbb{R}^r \times \mathbb{R}^r$.

As an example, given two vectors $u = [1, 2, 3, 4]^\top$ and $v = [5, 6, 7, 8]^\top$ the concatenated vectors are

$$(3.22) \quad [u, v]_0 = \begin{bmatrix} 1 \\ 5 \\ 2 \\ 6 \\ 3 \\ 3 \\ 7 \\ 4 \\ 8 \end{bmatrix}, \quad [u, v]_1 = \begin{bmatrix} 1 \\ 2 \\ 5 \\ 3 \\ 6 \\ 4 \\ 7 \\ 8 \end{bmatrix}, \quad [u, v]_2 = \begin{bmatrix} 1 \\ 2 \\ 3 \\ 5 \\ 4 \\ 6 \\ 7 \\ 8 \end{bmatrix}.$$

The operation simply permutes the entries and places them into a vector, so it is invertible. See [Figure 3.1](#) for a graphical illustration.

We will describe two permutations, the flattening permutation P_m^n , and the unflattening permutation Q_m^n , that will simplify the data for the summation operations by $S_{(m)}^n$.

We define a flattening permutation to a vector $P_m^n : \mathbb{R}^{E_{m-1}^n} \rightarrow \mathbb{R}^{|E_{m-1}^n|}$. First, we define the index

$$(3.23) \quad k_{\ell,t}^{(P)} := 2 \left(\sum_{\ell' < \ell} |E_{m,\ell'}^n| + \sum_{t' < t} |E_{m,\ell,t'}^n| \right), \quad t \in [2^m].$$

Then $P_m^n[f]$ for an image $f \in \mathbb{R}^{E_{m-1}^n}$ is defined entrywise as

$$(3.24) \quad (P_m^n[f])_{j+k_{\ell,t}^{(P)}} := \left([f_{m,2\ell,t}^n \mid f_{m,2\ell+1,t}^n]_t \right)_j, \\ j \in [k_{\ell,t+1}^{(P)} - k_{\ell,t}^{(P)}], \quad t \in [2^{n-m} - 1].$$

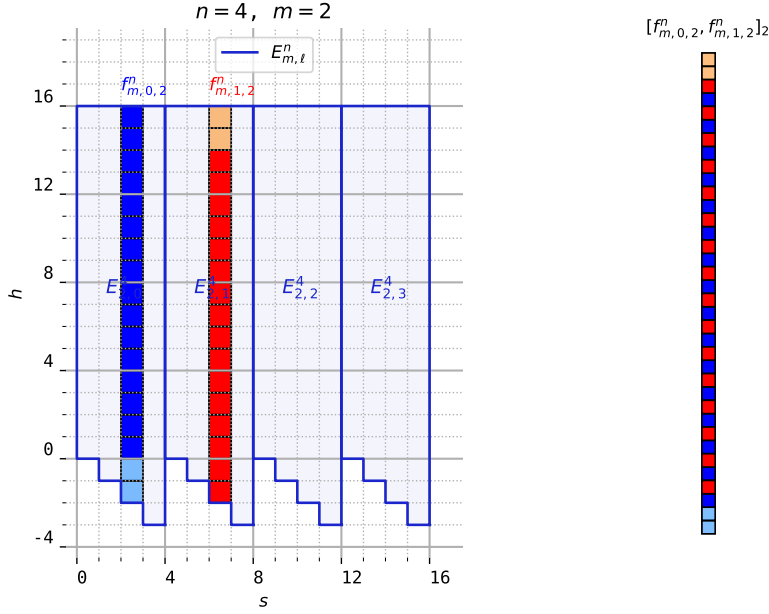


Fig. 3.2: Diagram depicting the flattening permutation P_m^n given in (3.24).

A diagram depicting the permutation P_m^n is shown in Figure 3.2.

Next, we define an unflattening permutation $Q_m^n : \mathbb{R}^{|E_m^n|} \rightarrow \mathbb{R}^{E_m^n}$. Define the index

$$(3.25) \quad k_{\ell,t}^{(Q)} := \sum_{\ell' < \ell} |E_{m,\ell'}^n| + \sum_{t' < 2t} |E_{m,\ell,t'}^n|, \quad t \in [2^{m-1}].$$

Let $Q_m^n[v] := g$ where the sections of the image g is given in terms of v by

$$(3.26) \quad [g_{m+1,\ell,2t}^n \mid g_{m+1,\ell,2t+1}^n] := \left[(v_{j+k_{\ell,2t}^{(Q)}})_{j \in [k_{m+1,\ell,t+1}^{(Q)} - k_{m+1,\ell,t}^{(Q)}]} \right]_0^{-1}$$

for $t \in [2^m - 1]$. A diagram depicting the permutation Q_m^n appears in Figure 3.3.

LEMMA 3.4 (Block convolution form). *A factor of the single-quadrant ADRT S_m^n in the case $m > 1$ can be written*

$$(3.27) \quad S_m^n = Q_m^n Z_m^n P_m^n,$$

where Z_m^n is given by (3.18), and the permutation matrices Q_m^n and P_m^n are given by (3.26) and (3.24), respectively.

Now, we know the SVD of Z_m^n (3.20) and how Z_m^n is related to S_m^n (3.27), thus the SVD of the single-quadrant factor S_m^n follows immediately: We have that

$$(3.28) \quad S_m^n = (Q_m^n U_m^n) \Sigma_m^n (P_m^n \top V_m^n)^\top, \quad m = 1, \dots, n.$$

It is easy to see that the SVD of the full ADRT factor $S_{(m)}^n$ follows too.

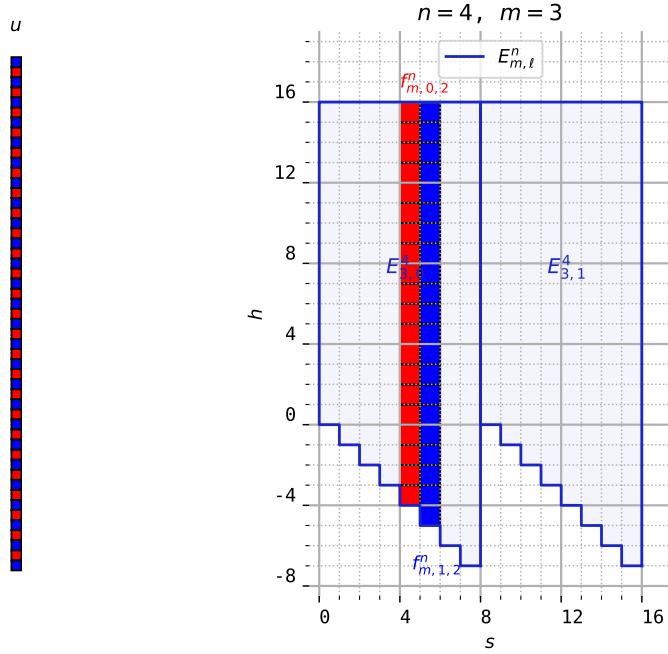


Fig. 3.3: Diagram depicting the unflattening permutation Q_m^n given in (3.26).

THEOREM 3.5 (SVD of $S_{(m)}^n$ for $m > 1$). *The SVD of $S_{(m)}^n$ up to the ordering of the singular values is given by*

$$(3.29) \quad S_{(m)}^n = U_{(m)}^n \Sigma_{(m)}^n V_{(m)}^{n\top}$$

where

$$(3.30) \quad \begin{cases} U_{(m)}^n := \text{Id}_4 \otimes (Q_m^n U_m^n), \\ \Sigma_{(m)}^n := \text{Id}_4 \otimes \Sigma_m^n, \\ V_{(m)}^n := \text{Id}_4 \otimes (P_m^{n\top} V_m^n). \end{cases}$$

The multiplication by each factor can be computed in at most $\mathcal{O}(N^2 \log N)$ operations.

Since $U_{(m)}^n$ and $V_{(m)}^n$ are made up of block matrices U_m^n and V_m^n , and these matrices are made up of columns from DST matrices, the complexity of multiplying by these matrices (or their transposes) is $\mathcal{O}(N^2 \log N)$.

4. Spectral decomposition of the cross-quadrant level ($m = 1$). Here we derive a spectral decomposition of the first factor $S_{(1)}^n$ (2.10) of ADRT (Definition 2.1). The technique required for the first level factor $S_{(1)}^n$ is different from the later levels; we discuss the difference and explain the difficulty. Regardless, we derive an alternative spectral decomposition by employing a block-sinusoidal decomposition of the original image.

4.1. Cross-quadrant level vs. single-quadrant levels. Recall that the first level factor $S_{(1)}^n$ of the ADRT flips and rotates the original image via the permutations

	(e, e)	(e, o)	(o, e)	(o, o)
Stencil	1 2 2 8 2 1	1 8 2 1 2 2	2 2 1 2 8 1	1 2 8 2 2 1
Quadrant I	1 1 2	2 1 1	1 1 2	2 1 1
Quadrant II	2 1 1	2 1 1	1 1 2	1 1 2
Quadrant III	1 2 1	1 2 1	1 2 1	1 2 1
Quadrant IV	1 1 2	2 1 1	1 1 2	2 1 1

Table 4.1: A description of the rows in $S_{(1)}^{n\top} S_{(1)}^n$. The first row shows the “stencil” of each row as categorized by whether the placement of the stencil has even or odd indexing in $[N/2] \times [N/2]$. The later rows detail the individual contributions coming from each of the four quadrants. These stencils are different depending on the row category, so $S_{(1)}^n$ is not a convolution.

T_I^n, \dots, T_{IV}^n (2.11). We illustrate below that these operations prevent $S_{(1)}^n$ from being a convolution-modulo-permutations. This fact implies that the convolution theorem (Lemma 3.1) cannot be applied to $S_{(1)}^n$ unlike in the later levels.

Let us compute the Gram matrix

$$(4.1) \quad S_{(1)}^{n\top} S_{(1)}^n \in \mathbb{R}^{N^2 \times N^2} \quad \text{where } N = 2^n,$$

and inspect the individual rows. We categorize each row depending on whether its index pair (a pair in the 2D-image-indexing $[N/2] \times [N/2]$) has even (e) or odd (o) number as its first and second indices. Then each row belongs to four possible categories depending on its index pair, $\{(e, e), (e, o), (o, e), (o, o)\}$. Reshaping the rows of each category (which are vectors in \mathbb{R}^{N^2}) into $N \times N$ images and displaying the non-zeros entries only, we obtain the 3×3 stencils shown in the first row of Table 4.1. There are four different types of stencils, so there is no clear convolutional structure.

Noting that the Gram matrix (4.1) can be expanded quadrant-wise

$$(4.2) \quad S_{(1)}^{n\top} S_{(1)}^n = \sum_{j \in \{I, \dots, IV\}} (S_1^n T_j^n)^\top (S_1^n T_j^n),$$

we also show in the subsequent rows in Table 4.1 the contributions from the individual terms, each coming from each of the four quadrants.

Again, there are four different types of stencils depending on the quadrant and the position of the row, so these individual operations are not convolutions. Naturally, the convolution theorem does not apply in this situation.

We can describe this difference of the first level $S_{(1)}^n$ another way. Consider the naïve inverse that can be derived from the SVD of the single-quadrant versions S_1^n (2.8). Recall that the single-quadrant ADRT at each level has the explicit SVD (3.28), e.g. for the first level we have $S_1^n = U_1^n \Sigma_1^n V_1^{n\top}$. Using this directly in the definition of $S_{(1)}^n$ (2.10), one derives a straightforward decomposition

$$(4.3) \quad S_{(1)}^n = (\text{Id}_4 \otimes U_1^n)(\text{Id}_4 \otimes \Sigma_1^n) [T_I^\top V_1^n \mid T_{II}^\top V_1^n \mid T_{III}^\top V_1^n \mid T_{IV}^\top V_1^n]^\top.$$

However, the last factor

$$(4.4) \quad [T_I^\top V_1^n \mid T_{II}^\top V_1^n \mid T_{III}^\top V_1^n \mid T_{IV}^\top V_1^n]$$

has orthogonal rows but non-orthogonal columns when viewed as a matrix: So this is not an SVD of $S_{(1)}^n$. Still, one can use this decomposition to compute the pseudo-inverse,

$$(4.5) \quad S_{(1)}^{n\dagger} = \frac{1}{4} [T_I \mid T_{II} \mid T_{III} \mid T_{IV}]^\top (\text{Id}_4 \otimes V_1^n) (\text{Id}_4 \otimes (\Sigma_1^n)^{-1}) (\text{Id}_4 \otimes U_1^{n\top}),$$

which amounts to computing the single-quadrant inverses for each quadrant separately, undoing the permutations T_I, \dots, T_{IV} , then averaging them pointwise. While this formula is algebraically correct, it has a downside in terms of its stability: the diagonal matrix $\text{Id}_4 \otimes (\Sigma_1^n)^{-1}$ contains large numerical values, similar to the later levels $\text{Id}_4 \otimes (\Sigma_m^n)^{-1}$. Therefore the stability of this naïve pseudo-inverse is equivalent to that of the exact inversion formula for the single-quadrant ADRT [14]; asymptotically, it is as unstable as the limited angle problem.

4.2. Spectral decomposition of $S_{(1)}^n$. Due to the observation laid out in the previous section, a different treatment is needed to derive a decomposition for $S_{(1)}^n$. Instead of relying on the convolution theorem Lemma 3.4, we derive an alternative explicit decomposition. The key idea is to construct a 2D version of the DST basis that are sinusoidal across 2×2 blocks rather than over individual entries.

We start by constructing a certain basis that will be useful. We decompose the linear space of images $\mathbb{R}^{N \times N}$ (where $N = 2^n$) defined on the grid $(i_1, i_2) \in [N] \times [N]$ into four different types indexed by $p \in [4]$.

Define $\chi_{(j_1, j_2)}^{(p)} : [N] \times [N] \rightarrow \mathbb{R}$ where $p \in [4]$ and $(j_1, j_2) \in [N/2] \times [N/2]$ by

$$(4.6) \quad \chi_{(j_1, j_2)}^{(0)}(i_1, i_2) = \begin{cases} 1 & \text{if } i_1 = j_1, i_2 = j_2, \\ 0 & \text{if } i_1 = j_1, i_2 = j_2 + 1, \\ 0 & \text{if } i_1 = j_1 + 1, i_2 = j_2, \\ 1 & \text{if } i_1 = j_1 + 1, i_2 = j_2 + 1, \\ 0 & \text{otherwise,} \end{cases}$$

$$(4.7) \quad \chi_{(j_1, j_2)}^{(1)}(i_1, i_2) = \begin{cases} -1 & \text{if } i_1 = j_1, i_2 = j_2, \\ 0 & \text{if } i_1 = j_1, i_2 = j_2 + 1, \\ 0 & \text{if } i_1 = j_1 + 1, i_2 = j_2, \\ 1 & \text{if } i_1 = j_1 + 1, i_2 = j_2 + 1, \\ 0 & \text{otherwise,} \end{cases}$$

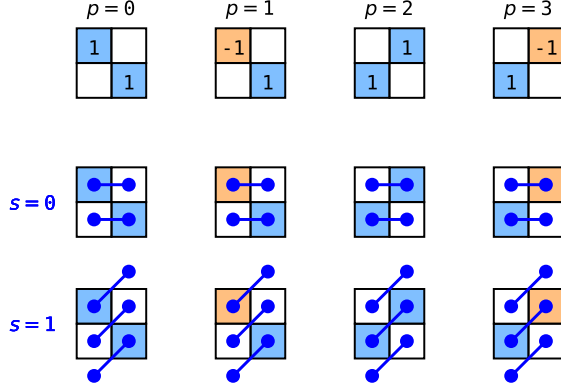


Fig. 4.1: The 2×2 blocks of the basis functions for each type $p \in [4]$.

$$(4.8) \quad \chi_{(j_1, j_2)}^{(2)}(i_1, i_2) = \begin{cases} 0 & \text{if } i_1 = j_1, i_2 = j_2, \\ 1 & \text{if } i_1 = j_1, i_2 = j_2 + 1 \\ 1 & \text{if } i_1 = j_1 + 1, i_2 = j_2, \\ 0 & \text{if } i_1 = j_1 + 1, i_2 = j_2 + 1, \\ 0 & \text{otherwise,} \end{cases}$$

$$(4.9) \quad \chi_{(j_1, j_2)}^{(3)}(i_1, i_2) = \begin{cases} 0 & \text{if } i_1 = j_1, i_2 = j_2, \\ -1 & \text{if } i_1 = j_1, i_2 = j_2 + 1 \\ 1 & \text{if } i_1 = j_1 + 1, i_2 = j_2, \\ 0 & \text{if } i_1 = j_1 + 1, i_2 = j_2 + 1, \\ 0 & \text{otherwise.} \end{cases}$$

Each of these basis functions are supported in 2×2 blocks. An illustration of the blocks is shown in [Figure 4.1](#).

Next, we define the set of functions $\chi^{(p)} \subset (\mathbb{R}^{N \times N})^{(N/2) \times (N/2)}$ based on their type p ,

$$(4.10) \quad \chi^{(p)} := \left\{ \chi_{(j_1, j_2)}^{(p)} \mid (j_1, j_2) \in [N/2] \times [N/2] \right\}, \quad p \in [4].$$

Then clearly, the union of their span is the linear space of $N \times N$ images,

$$(4.11) \quad \text{span} \bigcup_{p \in [4]} \chi^{(p)} = \mathbb{R}^{N \times N},$$

and these functions are pairwise orthogonal in the sense that

$$(4.12) \quad \sum_{(i_1, i_2) \in [N] \times [N]} \chi_{j_1, j_2}^{(p)}(i_1, i_2) \chi_{j'_1, j'_2}^{(p')}(i_1, i_2) = 2\delta_{pp'} \delta_{j_1 j'_1} \delta_{j_2 j'_2},$$

for $p, p' \in [4]$, $j_1, j'_1, j_2, j'_2 \in [N/2]$. Hence $\cup_{p \in [4]} \chi^{(p)}$ is an orthogonal basis for $\mathbb{R}^{N \times N}$.

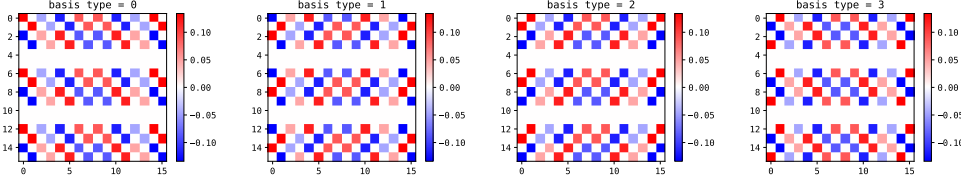


Fig. 4.2: An example of $v_{(k_1, k_2)}^{(p)}$ with $(k_1, k_2) = (5, 4)$ for each $p \in [4]$.

Next, we define certain sinusoidal functions. Let us define for each $(k_1, k_2) \in [N/2] \times [N/2]$ following basis functions for $\mathbb{R}^{N/2 \times N/2}$,

$$(4.13) \quad \phi_{(k_1, k_2)}(j_1, j_2) := \frac{1}{N+2} \sin\left(\frac{k_1 \pi j_1}{(N/2)+1}\right) \sin\left(\frac{k_2 \pi j_2}{(N/2)+1}\right),$$

and their variants

$$(4.14) \quad \begin{cases} \psi_{(k_1, k_2)}^{+\circ}(j_1, j_2) := \frac{c_{k_1}}{\sqrt{N+2}} \sin\left(\frac{k_1 \pi (j_1 + \frac{1}{2})}{(N/2)+1}\right) \sin\left(\frac{k_2 \pi j_2}{(N/2)+1}\right), \\ \psi_{(k_1, k_2)}^{\circ+}(j_1, j_2) := \frac{c_{k_2}}{\sqrt{N+2}} \sin\left(\frac{k_1 \pi j_1}{(N/2)+1}\right) \sin\left(\frac{k_2 \pi (j_2 + \frac{1}{2})}{(N/2)+1}\right), \\ \psi_{(k_1, k_2)}^{-\circ}(j_1, j_2) := \frac{c_{k_1}}{\sqrt{N+2}} \cos\left(\frac{k_1 \pi (j_1 + \frac{1}{2})}{(N/2)+1}\right) \sin\left(\frac{k_2 \pi j_2}{(N/2)+1}\right), \\ \psi_{(k_1, k_2)}^{\circ-}(j_1, j_2) := \frac{c_{k_2}}{\sqrt{N+2}} \sin\left(\frac{k_1 \pi j_1}{(N/2)+1}\right) \cos\left(\frac{k_2 \pi (j_2 + \frac{1}{2})}{(N/2)+1}\right), \end{cases}$$

in which c_k is the normalization factor for DCT-2 and DST-2,

$$(4.15) \quad c_k = \begin{cases} \frac{1}{\sqrt{N}} & \text{if } k = 0, \\ \frac{1}{\sqrt{2N}} & \text{otherwise.} \end{cases}$$

Finally, define the basis vectors $v_{(k_1, k_2)}^{(p)} : [N] \times [N] \rightarrow \mathbb{R}$ where $p \in [4]$ and $(k_1, k_2) \in [N/2] \times [N/2]$ given by

$$(4.16) \quad v_{(k_1, k_2)}^{(p)} = \frac{1}{\sqrt{2}} \sum_{(j_1, j_2) \in [N/2] \times [N/2]} \phi_{(k_1, k_2)}(j_1, j_2) \chi_{(j_1, j_2)}^{(p)}.$$

These functions are pairwise orthogonal in the sense that

$$(4.17) \quad \sum_{(i_1, i_2) \in [N] \times [N]} v_{k_1, k_2}^{(p)}(i_1, i_2) v_{k'_1, k'_2}^{(p')}(i_1, i_2) = \delta_{pp'} \delta_{k_1 k'_1} \delta_{k_2 k'_2},$$

for $p, p' \in [4]$, $k_1, k'_1, k_2, k'_2 \in [N/2]$. This basis will be used for our spectral decomposition.

Let O_1^n be a permutation of images in $\mathbb{R}^{|E_1^n|}$ reordering each columns into four blocks,

$$(4.18) \quad O_1^n v := \begin{bmatrix} w_1 \\ w_2 \\ w_3 \\ w_4 \end{bmatrix}, \quad w_1, w_2, w_3 \in \mathbb{R}^{N/2 \times N/2}, \quad w_4 \in \mathbb{R}^{((N/2)+1) \times N/2},$$

where the permuted entries are given by

$$(4.19) \quad \begin{aligned} (w_i)(j_1, j_2) &:= v((i \% 2) + 2(j_1 - 1), \lfloor i/2 \rfloor + j_2), \\ i \in [4]_1, \quad j_1 &\in \begin{cases} [N/2] & \text{if } i < 4 \\ [(N/2) + 1] & \text{if } i = 4 \end{cases}, \quad j_2 \in [N/2]. \end{aligned}$$

Since it is a permutation, its inverse is equal to its transpose, $(O_1^n)^{-1} = O_1^{n\top}$. We use this transpose in the following.

THEOREM 4.1 (Spectral decomposition of $S_{(1)}^n$). *We have the decomposition*

$$(4.20) \quad S_{(1)}^n = U_{(1)}^n \Sigma_{(1)}^n V_{(1)}^{n\top},$$

where the columns of $U_{(1)}^n$ and $V_{(1)}^n$ will be indexed by $(p, k_1, k_2) \in [4] \times [N/2] \times [N/2]$ and are given as follows: The columns of $V_{(1)}^n$ are $v_{(k_1, k_2)}^{(p)}$ (4.16) and the columns of $U_{(1)}^n$ are

$$(4.21) \quad u_{(k_1, k_2)}^{(p)} := \begin{bmatrix} O_1^{n\top} & & & \\ & O_1^{n\top} & & \\ & & O_1^{n\top} & \\ & & & O_1^{n\top} \end{bmatrix} w_{(k_1, k_2)}^{(p)}$$

where

$$(4.22) \quad \frac{1}{\sqrt{2}} \begin{bmatrix} w_{(k_1, k_2)}^{(0)} \\ \hline w_{(k_1, k_2)}^{(1)} \\ \hline w_{(k_1, k_2)}^{(2)} \\ \hline w_{(k_1, k_2)}^{(3)} \end{bmatrix} = \frac{1}{\sqrt{2}} \begin{bmatrix} w_{(k_1, k_2)}^{(0)} \\ \hline w_{(k_1, k_2)}^{(1)} \\ \hline w_{(k_1, k_2)}^{(2)} \\ \hline w_{(k_1, k_2)}^{(3)} \end{bmatrix}, \quad \frac{1}{\sqrt{2}} \begin{bmatrix} w_{(k_1, k_2)}^{(0)} \\ \hline w_{(k_1, k_2)}^{(1)} \\ \hline w_{(k_1, k_2)}^{(2)} \\ \hline w_{(k_1, k_2)}^{(3)} \end{bmatrix}, \quad \frac{1}{\sqrt{2}} \begin{bmatrix} w_{(k_1, k_2)}^{(0)} \\ \hline w_{(k_1, k_2)}^{(1)} \\ \hline w_{(k_1, k_2)}^{(2)} \\ \hline w_{(k_1, k_2)}^{(3)} \end{bmatrix}, \quad \frac{1}{\sqrt{2}} \begin{bmatrix} w_{(k_1, k_2)}^{(0)} \\ \hline w_{(k_1, k_2)}^{(1)} \\ \hline w_{(k_1, k_2)}^{(2)} \\ \hline w_{(k_1, k_2)}^{(3)} \end{bmatrix}.$$

The diagonal values of $\Sigma_{(1)}^n$ are given by

$$(4.23) \quad \begin{aligned} \sigma_{(k_1, k_2)}^{(0)} &= \sigma_{(k_1, k_2)}^{(2)} = \left(8 + \frac{1}{2}(\sigma_{k_1}^+)^2 + \frac{1}{2}(\sigma_{k_2}^+)^2 \right)^{\frac{1}{2}}, \\ \sigma_{(k_1, k_2)}^{(1)} &= \sigma_{(k_1, k_2)}^{(3)} = \left(4 + \frac{1}{2}(\sigma_{k_1}^-)^2 + \frac{1}{2}(\sigma_{k_2}^-)^2 \right)^{\frac{1}{2}}, \end{aligned}$$

where

$$(4.24) \quad \sigma_k^+ := 2 \cos\left(\frac{k\pi}{N+2}\right), \quad \sigma_k^- := 2 \sin\left(\frac{k\pi}{N+2}\right).$$

Proof. It suffices to consider the case for one basis type p and one quadrant, as the computation for the other cases are similar. We choose basis type $p = 3$ and quadrant I.

Fix $(k_1, k_2) \in [N/2] \times [N/2]$. Consider the permuted vector

$$(4.25) \quad T_I v_{(k_1, k_2)}^{(p)}.$$

Viewed as a 2D image, the 2×2 subblocks are now scalar multiples of the skew symmetric matrix

$$\begin{bmatrix} 0 & -1 \\ 1 & 0 \end{bmatrix}.$$

The calculation of the restriction of $u_{(k_1, k_2)}^{(p)}$ to quadrant I is simply

$$(4.26) \quad u_{(k_1, k_2)}^{(p)} \Big|_I (h, s) = [S_1^n T_I v_{(k_1, k_2)}^{(p)}] (h, s), \quad (h, s) \in E_1^n$$

can be decomposed into four parts, depending on whether h and s are each even or odd. We will consider each case.

When s is even, the sum occurs only within each subblock, and the sum is trivial since it adds zero to one entry in the subblock. So, when h is even, one obtains

$$(4.27) \quad u(h, s) = -\frac{1}{\sqrt{2}} \phi_{(k_1, k_2)}(\lfloor s/2 \rfloor, (N/2) - 1 - \lfloor h/2 \rfloor), \quad h \text{ even, } s \text{ even,}$$

and when h is odd,

$$(4.28) \quad u(h, s) = \frac{1}{\sqrt{2}} \phi_{(k_1, k_2)}(\lfloor s/2 \rfloor, (N/2) - 1 - \lfloor h/2 \rfloor), \quad h \text{ odd, } s \text{ even,}$$

Next, when s is odd and h is odd, we are only summing zero entries, so

$$(4.29) \quad u(h, s) = 0, \quad \text{for } h \text{ odd, } s \text{ odd,}$$

and finally when h is even,

$$(4.30) \quad \begin{aligned} u(h, s) &= \phi_{(k_1, k_2)}(\lfloor s/2 \rfloor, (N/2) - \lfloor h/2 \rfloor) - \phi_{(k_1, k_2)}(\lfloor s/2 \rfloor, (N/2) - 1 - \lfloor h/2 \rfloor) \\ &= -\sigma_{k_2}^- \psi_{(k_1, k_2)}^{\circ-}(\lfloor s/2 \rfloor, N/2 - \lfloor h/2 \rfloor), \end{aligned} \quad \square$$

by [Lemma 3.1](#). This calculation corresponds to the calculation of top four entries of $w_{(k_1, k_2)}^{(3)}$ in [\(4.22\)](#) (see [Figure 4.1](#) for a visual illustration.)

The diagonal values [\(4.23\)](#) are obtained by taking the ℓ^2 -norm of the vectors in [\(4.22\)](#).

5. Spectral pseudo-inverse of $S_{(1)}^n$. We finally turn to the problem of solving the system

$$(5.1) \quad S_{(1)}^n [x] = b, \quad b \in \text{range}(S_{(1)}^n).$$

Plugging in our spectral decomposition from [Theorem 4.1](#) we have

$$(5.2) \quad U_{(1)}^n \Sigma_{(1)}^n V_{(1)}^{n\top} x = b.$$

If this decomposition were the SVD, we would simply multiply by $U_{(1)}^{n\top}$ on both sides. Unfortunately, despite the notation resembling an SVD, the matrix $U_{(1)}^n$ here is not orthogonal in the standard inner product. It is not difficult to compute the Gram matrix associated with $U_{(1)}^n$ and see that it has the block matrix form

$$(5.3) \quad U_{(1)}^{n\top} U_{(1)}^n = \begin{bmatrix} \text{Id}_{N^2+N/2} & B_{12} & B_{13} & \\ B_{12}^\top & \text{Id}_{N^2+N/2} & & \\ B_{13}^\top & & \text{Id}_{N^2+N/2} & B_{34} \\ & & B_{34}^\top & \text{Id}_{N^2+N/2} \end{bmatrix}$$

where B_{13} is diagonal, the k -th diagonal of B_{21} are zero for k even. The blocks B_{21} and B_{34} only involve inner products between $\psi_{(k_1, k_2)}^{\pm\circ}$ and $\psi_{(k_1, k_2)}^{\circ\pm}$, and the diagonals of B_{21} are $|\phi_{(k_1, k_2)}^{(p)}|^2$ up to constant multiples. So the columns of U are orthogonal with respect to a weighted inner product, with the weight $(U_{(1)}^\top U_{(1)})^{-\frac{1}{2}}$, and this weight is not diagonal. So it might appear more work would be necessary to invert this system.

However, the solution can still be computed efficiently.

THEOREM 5.1 (Explicit spectral pseudo-inverse of $S_{(1)}^n$). *Given $b \in \text{range } S_{(1)}^n$ the linear problem solving for $x \in \mathbb{R}^{N^2}$ in*

$$(5.4) \quad S_{(1)}^n[x] = b$$

can be computed by applying two orthogonal transformations at the computational complexity $\mathcal{O}(N^2 \log N)$. More precisely, let $U_{(1)}^n, V_{(1)}^n$ be as in [Theorem 4.1](#) then the solution is given by

$$(5.5) \quad x = \widehat{V}_{(1)}^n \widehat{U}_{(1)}^{n\top} \widehat{b},$$

where the matrices on the RHS are defined by

$$(5.6) \quad \widehat{U}_{(1)}^n := M_{(1)}^n U_{(1)}^n \Sigma_{(1)}^n Q_{(1)}^n, \quad \widehat{V}_{(1)}^n := V_{(1)}^n Q_{(1)}^n, \quad \widehat{b} := M_{(1)}^n b,$$

and $M_{(1)}^n$ is a square diagonal matrix with 1s and 0s as entries (a truncation matrix), and $Q_{(1)}^n$ is an orthogonal matrix.

Proof. First, we derive the orthogonal matrix $\widehat{U}_{(1)}^n$, through a transformation of $U_{(1)}^n$. Denote by $\bar{w}_{(k_1, k_2)}^{(p)}$ the restriction of $w_{(k_1, k_2)}^{(p)}$ [\(4.22\)](#) where row-blocks involving the variants [\(4.14\)](#) are deleted. That is,

$$(5.7) \quad \frac{1}{\sqrt{2}} \begin{bmatrix} \bar{w}_{(k_1, k_2)}^{(0)} = \\ \phi_{(k_1, k_2)} \\ \phi_{(k_1, k_2)} \\ \hline 2\phi_{(k_1, k_2)} \\ \phi_{(k_1, k_2)} \\ \phi_{(k_1, k_2)} \\ \hline 2\phi_{(k_1, k_2)} \\ \phi_{(k_1, k_2)} \\ \phi_{(k_1, k_2)} \\ \hline \phi_{(k_1, k_2)} \\ \phi_{(k_1, k_2)} \end{bmatrix}, \quad \frac{1}{\sqrt{2}} \begin{bmatrix} \bar{w}_{(k_1, k_2)}^{(1)} = \\ \phi_{(k_1, k_2)} \\ -\phi_{(k_1, k_2)} \\ \hline \phi_{(k_1, k_2)} \\ -\phi_{(k_1, k_2)} \\ \hline -\phi_{(k_1, k_2)} \\ \phi_{(k_1, k_2)} \\ \hline \phi_{(k_1, k_2)} \\ -\phi_{(k_1, k_2)} \end{bmatrix}, \quad \frac{1}{\sqrt{2}} \begin{bmatrix} \bar{w}_{(k_1, k_2)}^{(2)} = \\ \phi_{(k_1, k_2)} \\ \phi_{(k_1, k_2)} \\ \hline \phi_{(k_1, k_2)} \\ \phi_{(k_1, k_2)} \\ \hline \phi_{(k_1, k_2)} \\ \phi_{(k_1, k_2)} \\ \hline 2\phi_{(k_1, k_2)} \\ \phi_{(k_1, k_2)} \\ \phi_{(k_1, k_2)} \\ \hline 2\phi_{(k_1, k_2)} \end{bmatrix}, \quad \frac{1}{\sqrt{2}} \begin{bmatrix} \bar{w}_{(k_1, k_2)}^{(3)} = \\ \phi_{(k_1, k_2)} \\ -\phi_{(k_1, k_2)} \\ \hline -\phi_{(k_1, k_2)} \\ \phi_{(k_1, k_2)} \\ \hline \phi_{(k_1, k_2)} \\ \phi_{(k_1, k_2)} \\ \hline \phi_{(k_1, k_2)} \\ -\phi_{(k_1, k_2)} \end{bmatrix}.$$

Then taking unit vectors in the directions

$$(5.8) \quad \begin{aligned} \hat{w}_{(k_1, k_2)}^{(0)} &\parallel \bar{w}_{(k_1, k_2)}^{(0)} + \bar{w}_{(k_1, k_2)}^{(2)}, & \|\hat{w}_{(k_1, k_2)}^{(0)}\|_2 &= 1, \\ \hat{w}_{(k_1, k_2)}^{(1)} &\parallel \bar{w}_{(k_1, k_2)}^{(1)}, & \|\hat{w}_{(k_1, k_2)}^{(1)}\|_2 &= 1, \\ \hat{w}_{(k_1, k_2)}^{(2)} &\parallel \bar{w}_{(k_1, k_2)}^{(0)} - \bar{w}_{(k_1, k_2)}^{(2)}, & \|\hat{w}_{(k_1, k_2)}^{(2)}\|_2 &= 1, \\ \hat{w}_{(k_1, k_2)}^{(3)} &\parallel \bar{w}_{(k_1, k_2)}^{(3)}, & \|\hat{w}_{(k_1, k_2)}^{(3)}\|_2 &= 1, \end{aligned}$$

where the notation $\cdot \parallel \cdot$ was used to denote that the two vectors are parallel, we obtain vectors given by

$$(5.9) \quad \begin{aligned} &\hat{w}_{(k_1, k_2)}^{(0)} \parallel \begin{bmatrix} \phi_{(k_1, k_2)} \\ \phi_{(k_1, k_2)} \\ \phi_{(k_1, k_2)} \\ \phi_{(k_1, k_2)} \\ \phi_{(k_1, k_2)} \\ \phi_{(k_1, k_2)} \\ \phi_{(k_1, k_2)} \\ \phi_{(k_1, k_2)} \\ \phi_{(k_1, k_2)} \\ \phi_{(k_1, k_2)} \end{bmatrix}, & & \hat{w}_{(k_1, k_2)}^{(1)} \parallel \begin{bmatrix} \phi_{(k_1, k_2)} \\ -\phi_{(k_1, k_2)} \\ \phi_{(k_1, k_2)} \\ -\phi_{(k_1, k_2)} \\ -\phi_{(k_1, k_2)} \\ \phi_{(k_1, k_2)} \\ \phi_{(k_1, k_2)} \\ \phi_{(k_1, k_2)} \\ -\phi_{(k_1, k_2)} \\ -\phi_{(k_1, k_2)} \end{bmatrix}, & & \hat{w}_{(k_1, k_2)}^{(2)} \parallel \begin{bmatrix} \phi_{(k_1, k_2)} \\ \phi_{(k_1, k_2)} \\ -\phi_{(k_1, k_2)} \\ \phi_{(k_1, k_2)} \\ -\phi_{(k_1, k_2)} \\ \phi_{(k_1, k_2)} \\ -\phi_{(k_1, k_2)} \\ \phi_{(k_1, k_2)} \\ -\phi_{(k_1, k_2)} \\ -\phi_{(k_1, k_2)} \end{bmatrix}, & & \hat{w}_{(k_1, k_2)}^{(3)} \parallel \begin{bmatrix} \phi_{(k_1, k_2)} \\ -\phi_{(k_1, k_2)} \\ -\phi_{(k_1, k_2)} \\ \phi_{(k_1, k_2)} \\ -\phi_{(k_1, k_2)} \\ -\phi_{(k_1, k_2)} \\ \phi_{(k_1, k_2)} \\ -\phi_{(k_1, k_2)} \\ \phi_{(k_1, k_2)} \\ -\phi_{(k_1, k_2)} \end{bmatrix}. \end{aligned}$$

The linear combinations in (5.8) is done by the matrix $Q_{(1)}^n$, and the normalization is achieved by a rescaling using the matrix $\Sigma_{(1)}^n$. That $\{\hat{w}_{(k_1, k_2)}^{(p)}\}_{p, k_1, k_2}$ forms an orthonormal set of vectors follows from direct calculation.

Then our original linear system (5.2) can be truncated,

$$(5.10) \quad M_{(1)}^n U_{(1)}^n \Sigma_{(1)}^n V_{(1)}^{n\top} x = M_{(1)}^n b.$$

Then, we rewrite

$$(5.11) \quad \underbrace{M_{(1)}^n U_{(1)}^n \Sigma_{(1)}^n Q_{(1)}^n}_{\hat{U}_{(1)}^n} \underbrace{Q_{(1)}^{n\top} V_{(1)}^{n\top}}_{\hat{V}_{(1)}^{n\top}} x = \hat{b},$$

and the orthogonal matrices on the LHS can be inverted, leading to (5.5). Since it is made up of blocks of DST, this computation can be done with complexity $\mathcal{O}(N^2 \log N)$. \square

Finally, using the SVD from Section 3 and the spectral decomposition from Section 4 we obtain the desired pseudo-inverse of the ADRT.

THEOREM 5.2 (Spectral Pseudo-Inverse, Fast and Explicit (SPIFE)). *Let $\hat{U}_{(1)}^n$ be as in Theorem 5.1, $V_{(1)}^n$ as in Theorem 4.1 and $U_{(m)}^n, \Sigma_{(m)}^n, V_{(m)}^n$ as in Theorem 3.5. Then a pseudo-inverse of R^n is given by*

$$(5.12) \quad (R^n)^\dagger = \hat{V}_{(1)}^n \hat{U}_{(1)}^{n\top} \prod_{m=2}^n V_{(m)}^n (\Sigma_{(m)}^n)^{-1} U_{(m)}^{n\top}.$$

The pseudo-inverse can be multiplied explicitly in $\mathcal{O}(N^2 \log^2 N)$ operations.

6. Numerical experiments. Here we conduct numerical experiments regarding SPIFE. We start by comparing the inversion result of five different methods:

<code>spife</code>	The pseudo-inverse using the spectral decomposition (5.12)
<code>spife-sq</code>	The pseudo-inverse using the single-quadrant SVDs and taking the average across four quadrants (4.5)
<code>cg</code>	The conjugate gradient (CG) iteration
<code>fmg</code>	The full multigrid (FMG) method
<code>alg</code>	The algebraically exact inversion formula

The implementation of the experiments was done using the open source Python software package `adrt` [15].

For useful comparisons, we run both the CG and FMG only up to $\log N$ iterations, so that the computational cost is comparable; both iterations cost at least $\sim N^2 \log N$ operations per iteration, so $\log N$ iterations result in the total cost of the order $\mathcal{O}(N^2 \log^2 N)$, the cost of our pseudo-inverse. Note however, `alg` has the slightly lower complexity $\mathcal{O}(N^2 \log N)$.

We try inverting various images from its ADRT data using these methods. The resulting inverse and the difference with the original image is shown in Figure 6.1. Three images are tested: a random 16×16 image where each pixel is drawn from $\mathcal{U}[-\frac{1}{2}, \frac{1}{2}]$, a smooth 128×128 image with size of sinusoidal wave packet with Gaussian amplitude, and an 128×128 image with size of a multilated Gaussian.

In all of the tested images, the error for `spife` is below `cg` and `fmg`, $1\text{e-}15$ for 16×16 images and below $1\text{e-}7$ for 128×128 images. `spife-sq` and `alg` behave similarly but have higher errors of a couple more orders of magnitude. `fmg` and `cg` have errors around $1\text{e-}1$ and $1\text{e-}2$ for 16×16 and $1\text{e-}4$ and $1\text{e-}5$ for 128×128 . In both cases, `fmg` has errors roughly an order of magnitude lower in comparison.

Next, we add different types of noise to the ADRT data above and observe how the accuracy of the inversion result changes. The noise perturbation causes the pseudo-inverse to deviate from the image, because now the ADRT data is no longer in $\text{range}(R^n)$. Throughout these experiments, the accuracy `cg` and `fmg` inverses are not affected; this is to be expected since these iterative schemes contain a projection to the range (These results also confirm that the noise perturbations are small enough so that the solution to the normal equations is still close to the original image).

We add uncorrelated uniform random noise of amplitude 0.1. The results are shown in the top row of Figure 6.2. `alg` show dramatic loss of accuracy, the errors render the image unrecognizable. `spife` inverse contains about $1\text{e-}1$ error performing better than `spife-sq` with errors around $6\text{e-}1$. This is attributable to the fact that cross-quadrant level $m = 1$ decomposition (Theorem 4.1) tends to project out the unstable modes, with a stabilizing effect.

We perturb the image with normal noise with $\sigma = 1\text{e-}5$. The results are shown in the middle row of Figure 6.2. In this case, the behavior is similar to that of the uniform noise. The difference between `spife` and `spife-sq` is more dramatic, due to the additional growth of an instability through 7 single-quadrant levels versus 4.

We perturb a single pixel in the ADRT data by adding to it a value of $1\text{e-}7$. The results are shown in the bottom row of Figure 6.2. This examples highlights the difference between `alg` and the new variants `spife` and `spife-sq`. The perturbed pixel does not affect the algebraically exact inverse, since the exact formula relies on

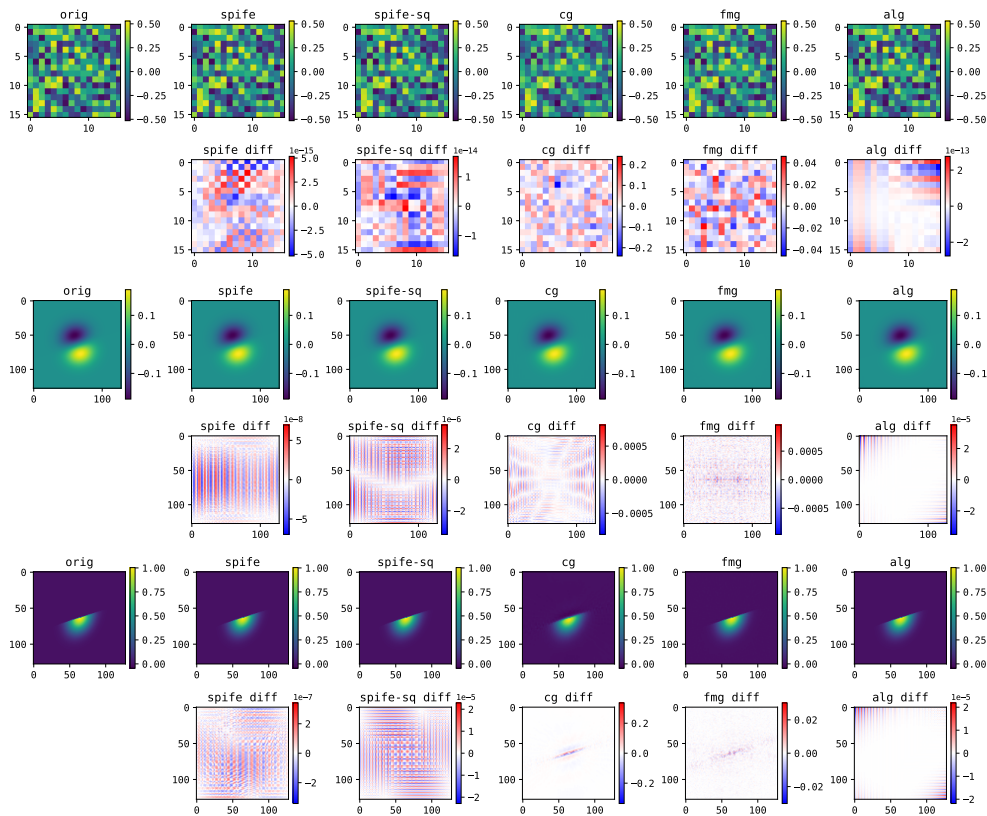


Fig. 6.1: Comparison of inversion results, for a random image (top row), smooth wave packet pulse (middle row), and multilobed Gaussian (bottom row).

local calculations and the perturbed pixel in this case is positioned in a way that the other pixels are not affected globally. For the spectral pseudo-inverses, however, the local perturbation effect is global, exciting high-frequency modes for the quadrant where the perturbed pixel was placed.

Taking the randomized image in the previous experiments (used in the top row of [Figure 6.2](#)), we perform a test for various noise levels. The result is shown in [Figure 6.3](#): **spife** is overall more accurate compared the other non-iterative inverses.

Finally, we illustrate the growth of numerical error during the repeated pseudo-inverses throughout the levels for the smooth image of higher resolution 256×256 , as shown in [Figure 6.4](#).

In broad terms, the spectral pseudo-inverse stabilizes the exact inversion formula, although the effect of data perturbation becomes global. For moderately small image sizes $N \leq 2^8$ the method yields superior accuracy when compared to both the CG iterations and full multigrid method, run with comparable computational cost. The growth of numerical errors in larger images suggest a need for a stabilization technique for the pseudo-inverse.

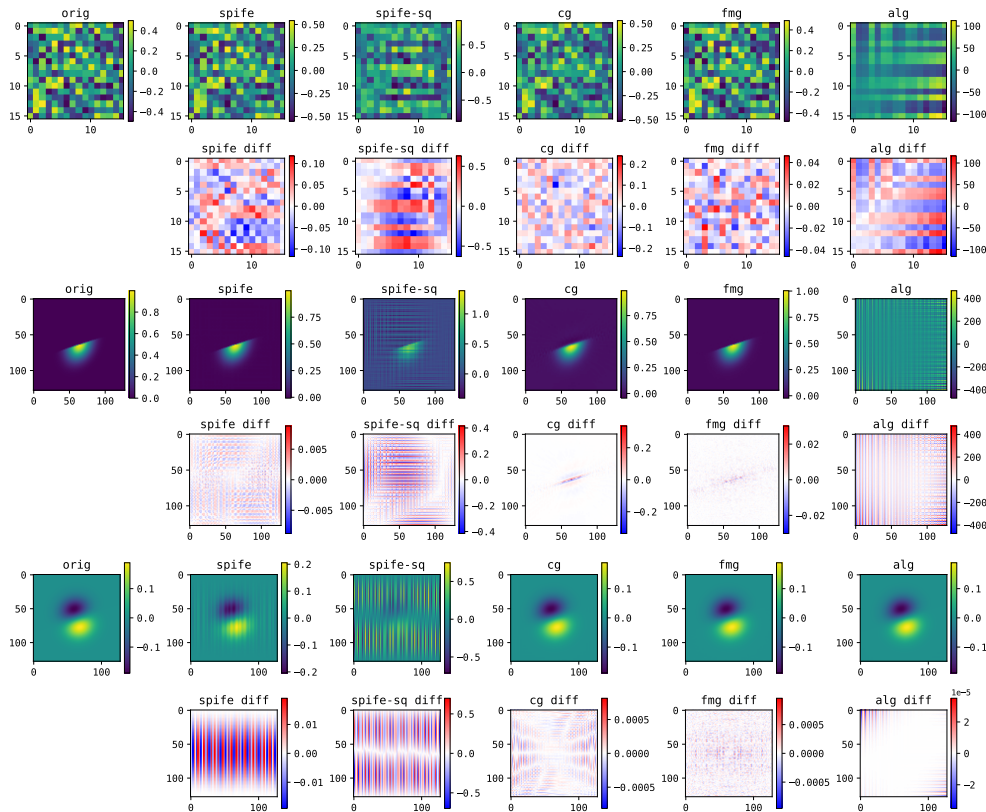


Fig. 6.2: Inversion results on the perturbed ADRT data. Result when uncorrelated uniform random noise level 0.1% was added to the data (top row), when uncorrelated random noise from normal distribution with $\sigma = 1e-5$ was added (middle row), when a single pixel was perturbed to amplitude $1e-7$ (bottom row).

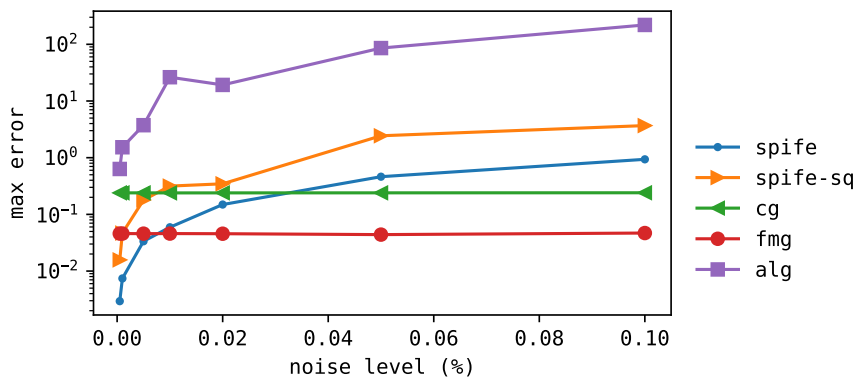


Fig. 6.3: Maximum error in the inverse for given noise level.

Acknowledgements. WL is supported by NSF-DMS Award #2309602, a PSC-CUNY grant, and a start-up fund from the Foundation for City College. Part of this work was done while DR was enjoying the hospitality of the International Research Institute of Disaster Science (IRIDeS) at Tohoku University supported by Invitational Fellowship Program for Collaborative Research with International Researcher (FY2023) hosted by Kenjiro Terada. The work of KR is partially supported by the NSF-DMS Award #1937254.

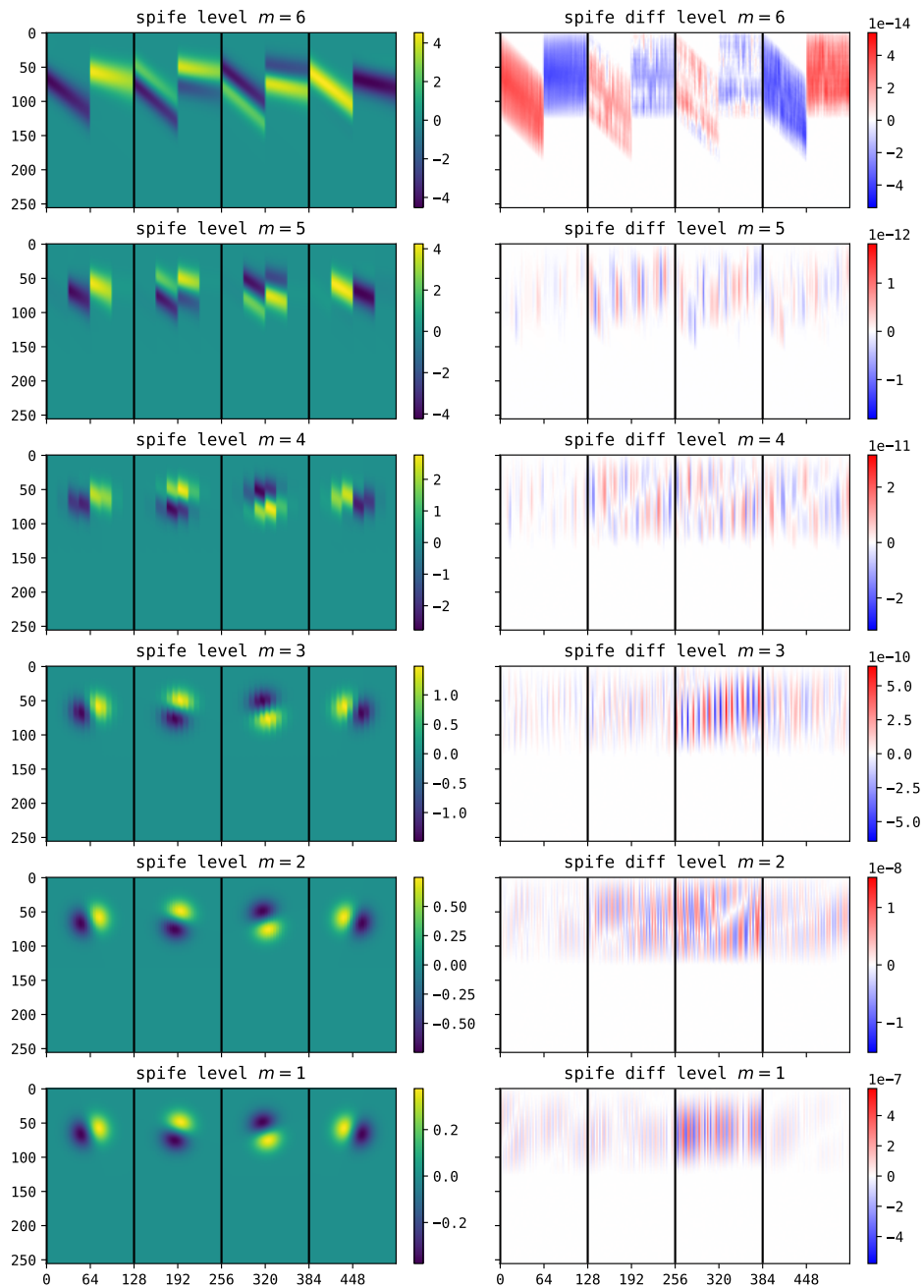


Fig. 6.4: Growth of numerical error during the intermediate levels during the pseudo-inverse `spife` (Theorem 5.2).

REFERENCES

- [1] A. AVERBUCH, R. R. COIFMAN, D. L. DONOHO, M. ISRAELI, AND Y. SHKOLNISKY, *A framework for discrete integral transformations I—the pseudopolar fourier transform*, SIAM Journal on Scientific Computing, 30 (2008), pp. 764–784.
- [2] A. AVERBUCH, R. R. COIFMAN, D. L. DONOHO, M. ISRAELI, Y. SHKOLNISKY, AND I. SEDELNIKOV, *A framework for discrete integral transformations II—the 2D discrete Radon transform*, SIAM Journal on Scientific Computing, 30 (2008), pp. 785–803.
- [3] A. AVERBUCH AND Y. SHKOLNISKY, *3D Fourier based discrete Radon transform*, Applied and Computational Harmonic Analysis, 15 (2003), pp. 33–69.
- [4] N. BONNEEL, J. RABIN, G. PEYRÉ, AND H. PFISTER, *Sliced and Radon Wasserstein barycenters of measures*, Journal of Mathematical Imaging and Vision, 51 (2015), pp. 22–45.
- [5] M. L. BRADY, *A fast discrete approximation algorithm for the Radon transform*, SIAM Journal on Computing, 27 (1998), pp. 107–119.
- [6] C. L. EPSTEIN, *Introduction to the Mathematics of Medical Imaging*, Society of Industrial and Applied Mathematics, 2007.
- [7] G. B. FOLLAND, *Introduction to Partial Differential Equations*, Princeton University Press, 2020.
- [8] W. GÖTZ AND H. DRUCKMÜLLER, *A fast digital radon transform: an efficient means for evaluating the hough transform*, Pattern Recognition, 29 (1996), pp. 711 – 718.
- [9] A. GREENBAUM, *Iterative Methods for Solving Linear Systems*, Society for Industrial and Applied Mathematics, 1997.
- [10] S. HELGASON, *Integral geometry and Radon transforms*, Springer, 2010.
- [11] W. LI, K. REN, AND D. RIM, *A range characterization of the single-quadrant ADRT*, Mathematics of Computation, 92 (2023), pp. 283–306.
- [12] A. K. LOUIS AND A. RIEDER, *Incomplete Data Problems in X-Ray Computerized Tomography*, Numerische Mathematik, 56 (1989), pp. 371–383.
- [13] F. NATTERER, *The Mathematics of Computerized Tomography*, Society for Industrial and Applied Mathematics, 2001.
- [14] R. OLIVA-GARCÍA, J. G. MARICHAL-HERNÁNDEZ, Ó. GÓMEZ-CÁRDENES, N. SUÁREZ-MARTÍN, AND J. M. RODRÍGUEZ-RAMOS, *A fast but ill-conditioned formal inverse to Radon transforms in 2D and 3D*, in Real-Time Image Processing and Deep Learning 2022, vol. 12102, International Society for Optics and Photonics, SPIE, 2022, p. 1210209.
- [15] K. OTNESS AND D. RIM, *adrt: approximate discrete Radon transform for Python*, Journal of Open Source Software, (2023), p. 5083.
- [16] W. H. PRESS, *Discrete Radon transform has an exact, fast inverse and generalizes to operations other than sums along lines*, Proceedings of the National Academy of Sciences, 103 (2006), pp. 19249–19254.
- [17] J. G. PROAKIS AND D. G. MANOLAKIS, *Digital Signal Processing (3rd Ed.): Principles, Algorithms, and Applications*, Prentice-Hall, Inc., USA, 1996.
- [18] D. RIM, *Dimensional splitting of hyperbolic partial differential equations using the Radon transform*, SIAM Journal on Scientific Computing, 40 (2018), pp. A4184–A4207.
- [19] D. RIM, *Exact and fast inversion of the approximate discrete Radon transform from partial data*, Applied Mathematics Letters, 102 (2020), p. 106159.
- [20] D. RIM AND K. MANDLI, *Displacement interpolation using monotone rearrangement*, SIAM/ASA Journal on Uncertainty Quantification, 6 (2018), pp. 1503–1531.
- [21] M. STÉPHANE, *A Wavelet Tour of Signal Processing (Third Edition)*, Academic Press, Boston, third edition ed., 2009.